**Key Points:**
- Steady quiet-time He-band EMIC waves are mostly observed in the morning-to-early afternoon sector
- The $f_{peak}/f_{H^+}$ values of the He-band waves are closer to $f_{O^+}$ than $f_{He^+}$
- The spectral properties of observed EMIC waves are in good agreement with the nonlinear wave growth theory

**Correspondence to:**
K.-H. Kim,
khan@khu.ac.kr

# Spectral characteristics of steady quiet-time EMIC waves observed at geosynchronous orbit

**Khan-Hyuk Kim[1,2], Jong-Sun Park[3], Yoshiharu Omura[2], Kazuo Shiokawa[4], Dong-Hun Lee[1], Gi-Jeong Kim[1], Ho Jin[1], Ensang Lee[1], and Hyuck-Jin Kwon[5]**

[1]School of Space Research, Kyung Hee University, Gyeonggi, South Korea, [2]Research Institute for Sustainable Humanosphere, Kyoto University, Kyoto, Japan, [3]Institute of Space Science, National Central University, Jhongli, Taiwan, [4]Institute for Space-Earth Environmental Research, Nagoya University, Nagoya, Japan, [5]Division of Climate Change Research, Korea Polar Research Institute, Incheon, South Korea

**Abstract** We have studied the spectral properties of quiet-time electromagnetic ion cyclotron (EMIC) waves following a steady quiet condition, which is defined with $Kp$ values $\leq 1$ during 12 h, using GOES 10, 11, and 12 magnetometer data for solar minimum years 2007–2008. We identified 6584 steady quiet-time EMIC wave samples using a semiautomated procedure. Approximately 82% of the samples were observed in the morning-to-early afternoon sector (0700–1500 magnetic local time) with a maximum occurrence near noon, and their peak frequencies were mostly in the He band. We found that the occurrence rate of steady quiet-time EMIC waves is higher than that of EMIC waves for all or quiet geomagnetic conditions ($Dst > 0$ nT or $AE < 100$ nT) reported in previous studies by a factor of 2 or more. The frequency ratio $f_{peak}$ (sample's peak frequency)/$f_{H^+}$ (the local proton gyrofrequency) of the He-band waves ($\sim 0.11$–$0.16$) under steady quiet conditions is lower than that ($\sim 0.14$–$0.24$) in previous studies. These results may be due to the fact that the plasmasphere expanded more frequently to the geosynchronous region under extremely quiet geomagnetic conditions in 2007–2008 than the periods selected in previous studies. The amplitude and frequency of He-band EMIC waves for nonlinear wave growth are examined as changing cold plasma density at geosynchronous orbit. We confirm that the spectral properties of observed EMIC waves are in good agreement with the nonlinear theory.

## 1. Introduction

The theory of wave-particle interactions [e.g., *Cornwall*, 1965; *Kennel and Petschek*, 1966] describes that proton (H⁺) cyclotron waves with frequencies below the proton gyrofrequency are generated as transverse left-handed polarized waves in the equatorial region of the magnetosphere beyond $L = 4$ by the proton cyclotron instability. The source of free energy for this instability is anisotropic ($T_\perp > T_\parallel$), where $T_\perp$ and $T_\parallel$ are perpendicular and parallel temperatures, respectively, to the background magnetic field, and energetic ($\sim 10$–$100$ keV) protons injected into the Earth's magnetosphere.

The Earth's magnetosphere is filled with energetic ring current plasmas and cold plasmaspheric plasmas, both of which contain heavy ions (primarily O⁺ and He⁺). The presence of heavy ions even in small quantities dramatically modifies the amplification and propagation of waves generated by wave-particle interactions [e.g., *Young et al.*, 1981; *Kozyra et al.*, 1984]. In the presence of cold heavy ions these waves appear in three distinct bands, H band between the local H⁺ gyrofrequency ($f_{H^+}$) and He⁺ gyrofrequency ($f_{He^+}$), He band between the local He⁺ gyrofrequency ($f_{He^+}$) and O⁺ gyrofrequency ($f_{O^+}$), and O band below $f_{O^+}$, and are now known as electromagnetic ion cyclotron (EMIC) waves.

EMIC waves are commonly observed in space over a wide $L$ range [*Anderson et al.*, 1992a; *Fraser and Nguyen*, 2001; *Min et al.*, 2012; *Usanova et al.*, 2012; *Keika et al.*, 2013; *Meredith et al.*, 2014] and also on the ground at low to high latitudes [e.g., *Fraser et al.*, 1989; *Engebretson et al.*, 2002; *Nomura et al.*, 2011; *Kim et al.*, 2016] in the frequency range of Pc1–Pc2 pulsations ($\sim 0.1$–$5$ Hz). Theoretical studies suggest that the greatest amplification of EMIC waves occurs near the geomagnetic equator where the magnetic field strength is minimum and the cold plasma density is high [e.g., *Cornwall*, 1965; *Kennel and Petschek*, 1966; *Kozyra et al.*, 1984; *Mauk*, 1982]. The relationship between the occurrence of EMIC waves and enhancement in cold plasma density has led to a prediction that the afternoon-to-dusk sector in the outer magnetosphere, where energetic/anisotropic

ring current or plasma sheet ions drifting westward interact with cold and dense plasmas in the plasmaspheric bulge and plumes, is a favored region for the generation of EMIC waves. It has been reported that plasmaspheric plumes have a high chance of being detected in the afternoon sector between $L=6$ and $L=9$ [*Darrouzet et al.*, 2008]. The high occurrence of EMIC waves at $L > 7$ in the afternoon sector from Active Magnetospheric Particle Tracer Explorers (AMPTE)/CCE [*Anderson et al.*, 1992a; *Keika et al.*, 2013] and Time History of Events and Macroscale Interactions during Substorms (THEMIS) [*Min et al.*, 2012; *Usanova et al.*, 2012] observations is consistent with the theoretical prediction that growth rate can be expected to increase with radial distance [e.g., *Anderson et al.*, 1992a].

Anisotropic ($T_\perp > T_\parallel$) ions providing free energy for EMIC instability are convected and injected toward the inner magnetosphere, respectively, during geomagnetic storms [e.g., *Erlandson and Ukhorskiy*, 2001; *Meredith et al.*, 2003; *Fraser et al.*, 2010; *Halford et al.*, 2010] and substorms [e.g., *Ishida et al.*, 1987]. Such an anisotropic condition for EMIC wave generation can also be expected when the magnetosphere is compressed by large solar wind dynamic pressure changes associated with sudden commencements [e.g., *Olson and Lee*, 1983; *Anderson and Hamilton*, 1993; *Engebretson et al.*, 2002; *Arnoldy et al.*, 2005; *Usanova et al.*, 2008] and even by small changes in the solar wind dynamic pressure during quiet geomagnetic conditions [*Hyun et al.*, 2014; *Park et al.*, 2016].

Since EMIC waves interact with energetic ring current ions and relativistic electrons and cause loss of these particles into the Earth's atmosphere through pitch angle scattering [e.g., *Kennel and Petschek*, 1966; *Thorne and Kennel*, 1971; *Erlandson and Ukhorskiy*, 2001; *Summers and Thorne*, 2003], their activities are critical to the dynamics of ring current and radiation belt particles, in particular for MeV electrons [e.g., *Horne*, 2002; *Summers and Thorne*, 2003; *Kang et al.*, 2015]. Observations of precipitating ring current or radian belt particles at low-altitude polar-orbiting spacecraft during the occurrence of EMIC waves support the theory of resonant wave-particle interactions with EMIC waves [e.g., *Yahnina et al.*, 2000; *Miyoshi et al.*, 2008; *Yuan et al.*, 2012; *Hyun et al.*, 2014; *Kim et al.*, 2016].

In a recent study reported by *Park et al.* [2016], who used geosynchronous magnetic field data in 2007–2008, the authors confined their attention only to geomagnetically quiet periods ($Kp \leq 1$). Within this limitation they found that the He-band EMIC waves at geosynchronous orbit mostly occur in the morning-to-early afternoon sector (0700–1500 magnetic local time, MLT) with a peak around noon, which is clearly different from previous results for all $Kp$ conditions showing a peak occurrence in the afternoon around 1500–1600 magnetic local time (MLT) [*Anderson et al.*, 1992a; *Clausen et al.*, 2011; *Min et al.*, 2012; *Usanova et al.*, 2012; *Keika et al.*, 2013]. They also found that solar wind dynamic pressure enhancement is a main control parameter for quiet-time EMIC wave occurrence and that the amplitude of the pressure enhancement need not be large for excitation of the EMIC waves.

This paper extends the study by *Park et al.* [2016], called P1, to examine spectral characteristics of quiet-time EMIC waves. As mentioned above the presence of heavy ions in the cold plasmaspheric plasma strongly affects EMIC wave properties. Under moderate geomagnetic conditions the plasmapause is located near $L \sim 4$–$5$ and thus geosynchronous orbit is mostly outside the plasmapause. Under quiet conditions, however, the plasmapause expands to or even beyond geosynchronous orbit [e.g., *Kwon et al.*, 2015]. This indicates that the dense and cold plasmaspheric plasma appears more frequently at the geosynchronous region during the solar minimum period 2007–2008 selected in our study. By comparing with previous results, we discuss whether spectral characteristics of quiet-time EMIC waves are due to heavy ions in the cold plasmaspheric plasma.

This paper is organized as follows. In section 2 we describe the data set for this study. In section 3 we present samples of steady quiet-time EMIC waves. In section 4 we present the statistical analysis. In section 5 we discuss the statistical results, and conclusions are presented in section 6.

## 2. Data Set

We use high time resolution (∼0.512 s) magnetic field data from GOES 10, GOES 11, and GOES 12 acquired through a 2 year period from January 2007 to December 2008 in order to identify geosynchronous EMIC waves. The GOES magnetic field vector quantities are presented in a mean-field-aligned (MFA) coordinate system in order to separate the compressional and transverse components. The data set and coordinate system used in this study are in the same format as those used in P1. Detailed descriptions of the data processing and coordinate system are given in P1.
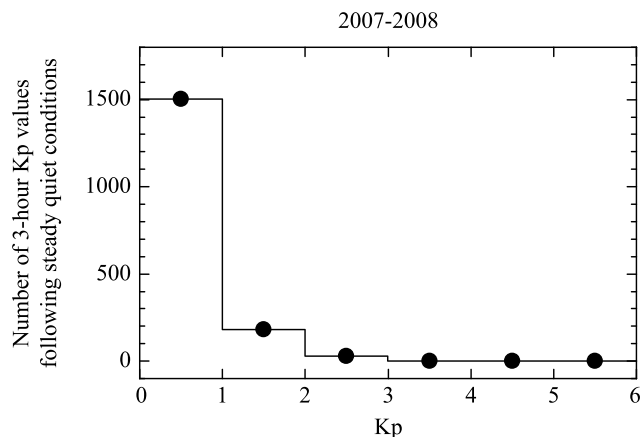
**Figure 1.** Occurrence frequency distribution of the 3 h $Kp$ values following steady quiet conditions during the period of 2007–2008. Most of $Kp$ values (~88%) immediately following steady quiet conditions were between 0 and 1.

The quiet-time EMIC wave events presented in P1 were selected when geomagnetic activity was low ($Kp \leq 1$) without considering geomagnetic conditions before the onset of the events. Because there may be a variety of $Kp$ values just before the onset of quiet-time EMIC waves, some of the events in P1 would not have a connection to quiet geomagnetic conditions. To ensure that EMIC wave events are associated with quiet conditions, we selected the events following a steady quiet condition, which is defined with $Kp$ values $\leq 1$ during 12 h. That is, the maximum $Kp$ was $\leq 1$ for the four 3 h $Kp$ values (12 h) prior to the event that occurred for any interval of $Kp \leq 1$. Figure 1 shows the occurrence frequency distribution of the $Kp$ values following steady quiet conditions during the period of 2007–2008. Most of $Kp$ values (~88%) immediately following steady quiet conditions were between 0 and 1. In this study, we use the GOES magnetic field records for such intervals to identify steady quiet-time EMIC waves.

## 3. Example of Steady Quiet-Time EMIC Waves
### 3.1. Dynamic Spectra of EMIC Waves
Figure 2 shows the $Kp$ index, solar wind dynamic pressure ($P_{sw}$), and $AE$ index for a 2 day period (2–3 July) in 2008. $P_{sw}$ was calculated with the solar wind parameters (solar wind speed and density), time shifted to the bow shock nose, from the Wind spacecraft. During most of the interval of the 2 day period, the $Kp$ index was at low levels $\leq 1$, and the $AE$ index was less than 50 nT. $P_{sw}$ was near ~1 nPa. The $Kp$ index slightly increased to 1+ for 15:00–18:00 UT on 3 July. This is due to a small but sudden increase in $P_{sw}$ around 12:00 UT and a small substorm activity associated with a peak amplitude of ~160 nT in $AE$ around 16:00 UT. After 18:00 UT on the same day, $Kp$ decreased again to the low level less than 1. Since the steady quiet condition is defined as the 12 h interval with the maximum $Kp \leq 1$, the 3 h $Kp$ intervals following the steady quiet conditions are in the period from 15:00 UT on 2 July to 18:00 UT on 3 July. This period is marked by the thick horizontal bar in Figure 2a.

Figures 3a and 3b display the dynamic power spectra of the transverse components, $\delta b_x$ and $\delta b_y$, in MFA coordinates with the local helium ($f_{He^+}$) and oxygen ($f_{O^+}$) gyrofrequencies at the GOES 10 spacecraft for the interval from 09:00 to 21:00 UT on 3 July 2008, highlighted by shading in Figure 2. The spectra were generated by Fourier transforming for the interval with the same method as that used in P1 without time differencing. GOES 10 dynamic spectra show the He-band EMIC waves enhanced in the frequency band between $f_{He^+}$ and $f_{O^+}$ for the interval of ~10:40–19:00 UT. During this EMIC wave interval GOES 10 moved from dawn (MLT =~6.4 h) to afternoon (MLT =~15.2 h) on geosynchronous orbit. The spectral intensity in $\delta b_x$ is strongly time modulated with large wave activity for the intervals of ~13:00–14:30 UT and ~16:00–17:00 UT. The intensity modulation in $\delta b_y$ is fairly similar to that in $\delta b_x$, but not the same. As shown in Figure 2, $P_{sw}$ was enhanced between 12:00 UT and 19:00 UT. This implies that the quiet-time EMIC waves are triggered by $P_{sw}$ variations when GOES 10 was in the morning and dayside [Hyun et al., 2014; Park et al., 2016]. However, we do not exclude the possibility that the occurrence of the EMIC waves was associated with substorm activity [Ishida et al., 1987] because a sudden increase in $AE$ occurred around 15:00 UT.
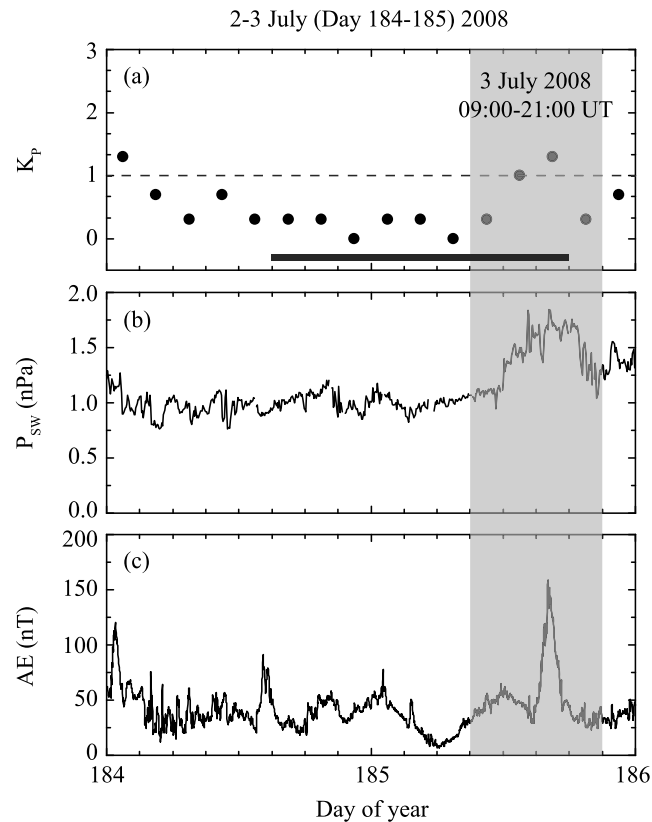
**Figure 2.** (a) The $Kp$ index, (b) solar wind dynamic pressure ($P_{sw}$), and (c) $AE$ index for a 2 day period (2–3 July) in 2008. The steady quiet condition is defined as the 12 h interval with the maximum $Kp \leq 1$. The thick horizontal bar indicates a period including the 3 h $Kp$ intervals following the steady quiet conditions. The shading indicates a period selected for detailed EMIC waves analysis in Figures 3 and 6.

Figures 3c shows the $\delta b_x$-$\delta b_y$ coherence spectra. The coherence is defined as

$$\gamma = \frac{|G_{xy}|^2}{G_{xx}G_{yy}} \tag{1}$$

where $G_{xx}$ and $G_{yy}$ are the autospectral density (or power spectral density) functions of time series $x(t)$ and $y(t)$, respectively, and $G_{xy}$ is the cross-spectral density function between $x(t)$ and $y(t)$ [*Bendat and Piersol*, 2010]. If $\gamma$ is unity, $x(t)$ and $y(t)$ are completely identical. If $\gamma$ is zero, both time series data are completely unrelated. Thus, the value of the coherence function indicates how much of $x(t)$ is related to $y(t)$ and determines the similarity in waveform between two signals. Since $\gamma$ depends on the cross-spectral density function given as the product of the Fourier transforms of $x(t)$ and $y(t)$, the relative phase of two signals should be constant for high coherence.

When the $\delta b_x$ and $\delta b_y$ dynamic spectra are compared, it is evident that there is a high degree of spectral similarity between both transverse components in terms of the spectral intensity modulation in the He band. However, the $\delta b_x$-$\delta b_y$ coherence is significantly low for the enhanced EMIC wave intervals, although there are a few intervals of high coherence, for example, ~10:40–11:20 UT and ~13:00–14:00 UT. This indicates that oscillations in $\delta b_x$ and $\delta b_y$ are coherent only for a fraction of the EMIC wave intervals. As mentioned above, the phase delay between two signals needs to remain constant to produce a strong coherence. Thus, our observations of low-coherence intervals can be interpreted as $\delta b_x$ and $\delta b_y$ oscillated with slightly different frequencies. That is, the relative phase variations of $\delta b_x$ and $\delta b_y$ are incoherent.

Figure 3d shows the degree of polarization derived from the $\delta b_x$ and $\delta b_y$ time series. We used the method described by *Fowler et al.* [1967] to determine the degree of polarization ($R$) defined as

$$R = \left[1 - \frac{4|G|}{(G_{xx} + G_{yy})^2}\right]^{1/2} = \left[1 - \frac{4(G_{xx}G_{yy} - G_{xy}G_{xy}^*)}{(G_{xx} + G_{yy})^2}\right]^{1/2} \tag{2}$$
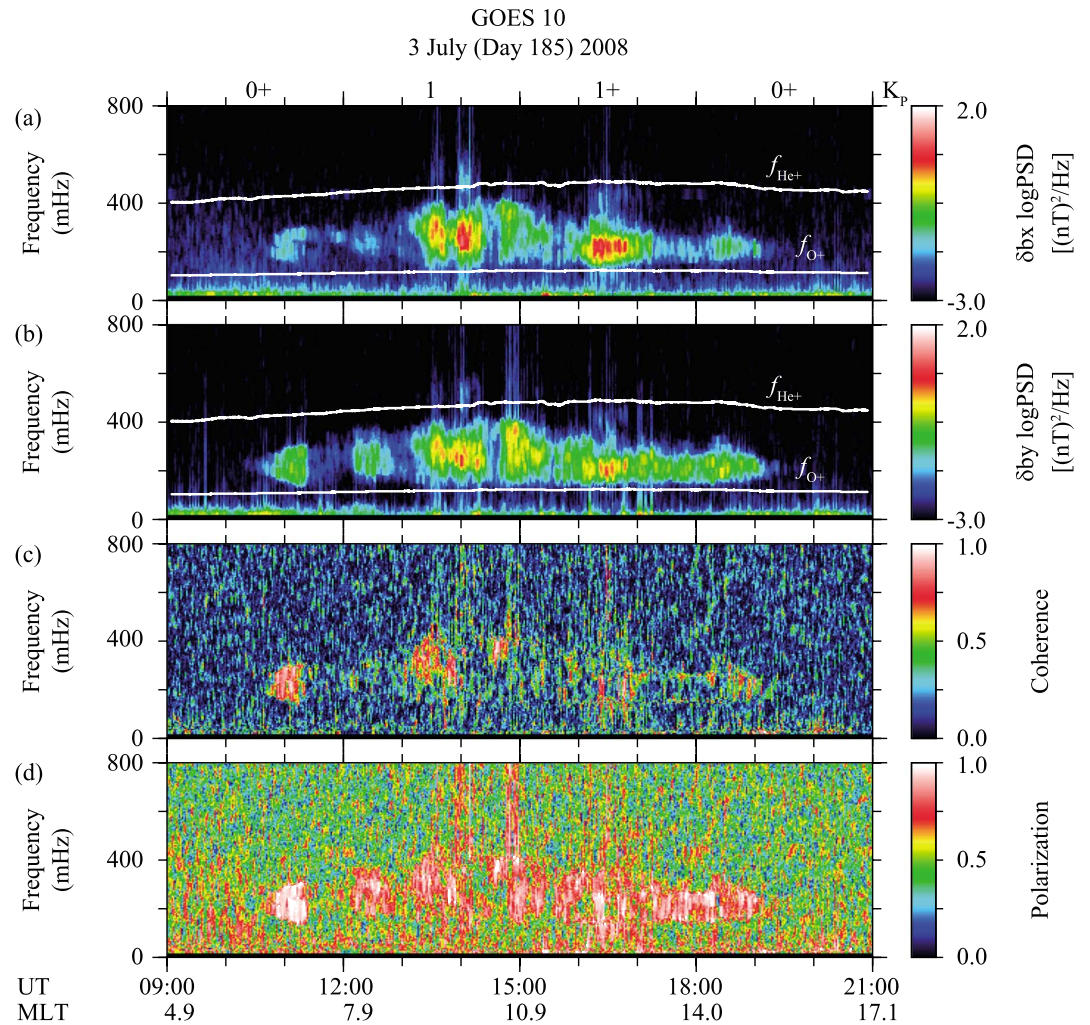
**Figure 3.** Dynamic power spectra of the transverse components, (a) $\delta b_x$ and (b) $\delta b_y$, in a mean-field-aligned coordinate system at the GOES 10 spacecraft for the interval from 09:00 to 21:00 UT on 3 July 2008. Two white lines indicate the local helium ($f_{He+}$) and oxygen ($f_{O+}$) gyrofrequencies, respectively. (c) The $\delta b_x$-$\delta b_y$ coherence spectra. (d) The degree of polarization derived from the $\delta b_x$ and $\delta b_y$ time series.

where $|G|$ is the determinant of a coherency matrix of a two-component time series $x(t)$ and $y(t)$ and the asterisk denotes the complex conjugate. Using the definition of $\gamma$ in (1), $R$ is given as

$$R = \left[ 1 - \frac{4(1-\gamma)G_{xx}G_{yy}}{(G_{xx} + G_{yy})^2} \right]^{1/2} \tag{3}$$

If $\gamma$ is unity, the signals of $x(t)$ and $y(t)$ consist of a completely polarized signal (i.e., $R = 1$). If $\gamma$ is zero, however, $R$ is zero only in the case of $G_{xx} = G_{yy}$. $R$, defined from (3), will increase if any oscillation existing in only $x(t)$ or $y(t)$ dominates the coherency matrix even though $\gamma$ is zero. This problem is due to the fact that the time series $x(t)$ and $y(t)$ in $R$ are assigned the same frequency. Thus, we suggest that $\gamma$ should be examined with $R$ prior to determining polarization characteristics of waves. In (3), $R = (\gamma)^{0.5}$ when the amplitudes of two signals are identical (i.e., $G_{xx} = G_{yy}$). In this study the high coherence is defined to be $\gamma > 0.7$, and the high degree of polarization is defined to be $R > 0.8$.

Unlike the $\delta b_x - \delta b_y$ coherence, the degree of polarization displayed in Figure 3d is persistently high in the entire band for spectral enhancements of EMIC waves. For example, the coherence in the intervals, ~12:10–12:50 UT and ~17:00–19:00 UT, is significantly low, but the degree of the polarization is very high ($R > 0.8$). This high degree of polarization is not due to a strongly polarized signal but a large-amplitude
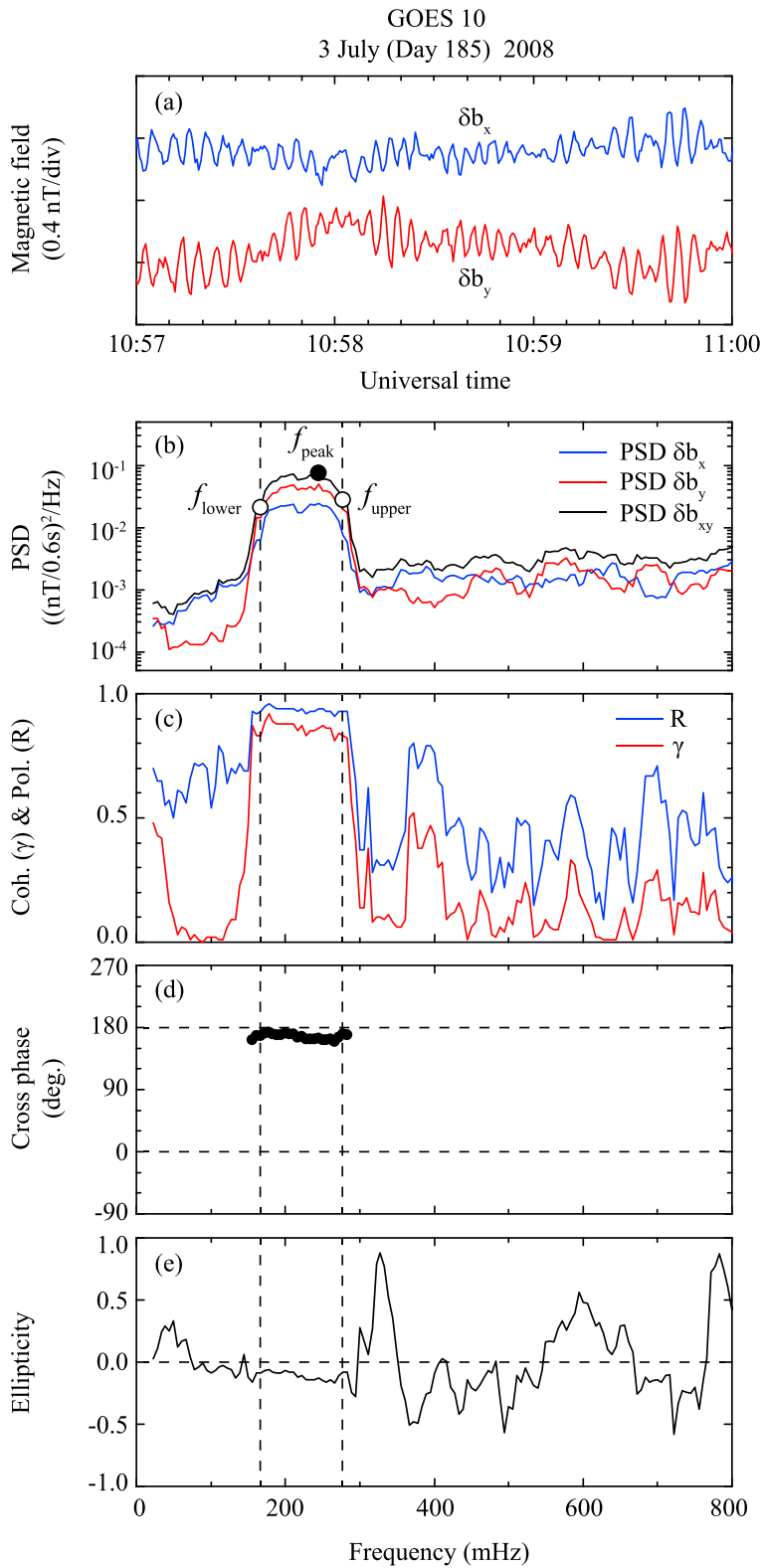
**Figure 4.** (a) The time series of the transverse magnetic field components, $\delta b_x$ (blue) and $\delta b_y$ (red), for a 3 min period 10:57–11:00 UT on 3 July 2008. Spectral parameters computed from the time series: (b) the transverse power spectral densities (PSD $\delta b_x$ and PSD $\delta b_x$) and total transverse power spectral density (PSD $\delta b_{xy}$), (c) coherence (red) and degree of polarization (blue), (d) cross phase, and (e) ellipticity. The enhanced spectral width is marked by the two vertical dashed lines.

difference between $\delta b_x$ and $\delta b_y$. That is, $\delta b_x$ or $\delta b_y$ oscillations dominate a two-dimensional vector signal in the x-y plane, which is perpendicular to the ambient background magnetic field. The coherence and degree of polarization are high in the interval of ~10:40–11:20 UT, indicating that the EMIC waves are highly polarized.

### 3.2. Spectral Analysis and EMIC Wave Detection Method

Figure 4a shows the time series of the transverse magnetic field components, $\delta b_x$ and $\delta b_y$, for a 3 min period (10:57–11:00 UT) selected from the high coherence and polarization interval of EMIC waves seen in Figure 3. Although the spectral intensity for the interval is weak as shown in Figure 3, the coherence and degree of polarization are high. This indicates that the coherence and polarization do not depend on the wave amplitude. The two traces show quite similar wave packet structures with comparable amplitudes. $\delta b_x$ and $\delta b_y$ oscillate, maintaining a 180° phase delay throughout the 3 min period. Figures 4b–4e show the transverse power spectral densities (PSD_$\delta b_x$ and PSD_$\delta b_y$), total transverse power spectral density (PSD_$\delta b_{xy}$) defined to be PSD_$\delta b_x$+ PSD_$\delta b_y$, coherence ($\gamma$), degree of polarization ($R$), cross phase, and ellipticity as a function of frequency. As shown in the time series plot, each component had a variation much slower in period and larger in amplitude than EMIC wave oscillations. To remove such slowly varying magnetic fields, the time series was time differenced prior to Fourier transform. The cross-phase estimates are shown only if the coherence is higher than 0.7. The ellipticity is defined to be the ratio of the minor to major axes of the ellipse as described by *Fowler et al.* [1967]. If the ellipticity is 0 ($\pm1$), the wave is linearly (circularly) polarized. The value of the ellipticity lies between −1 and 1. The negative (positive) sign of the ellipticity corresponds to left-handed (right-handed) polarization when looking into the direction of the background magnetic field.

In order to identify EMIC wave samples and examine their spectral properties, we determine the highest spectral peak in PSD_$\delta b_{xy}$ and the spectral width of the peak at the PSD_$\delta b_{xy}$ level that is 50% of the peak power (i.e., the full width at half maximum). The spectral peak (marked by a solid circle, $f_{peak}$) and its width (marked by open circles, $f_{lower}$ and $f_{upper}$) for the PSD_$\delta b_{xy}$ of the 3 min time series are plotted in Figure 4b. As expected from the time series, spectral shapes of $\delta b_x$ and $\delta b_y$ are very similar. The coherence and polarization are high ($\gamma > 0.8$ and $R > 0.9$) in the frequency band of ~165–280 mHz. In that frequency band, the cross phase is near 180°, and the ellipticity is close to zero, indicating a linear polarization.

Figure 5 shows the low-coherence time series of the transverse components and spectral properties for two 3 min intervals, 12:17–12:20 UT, 14:03–14:06 UT, and 16:01–16:04 UT, in the same format as for Figure 4. The oscillations in $\delta b_x$ and $\delta b_y$ for 12:17–12:20 UT in Figure 5a are likely to have similar periods. In the expanded time scale (not shown here), however, we find that the phase delay between $\delta b_x$ and $\delta b_y$ is not constant throughout the 3 min interval. That is, the oscillations were in phase (marked by solid cycles) and then became out of phase (marked by open cycles) after several cycles. This indicates that $\delta b_x$ and $\delta b_y$ oscillate with slightly different frequencies. Consequently, the spectral peaks of $\delta b_x$ and $\delta b_y$ appear at different frequencies. The coherence calculated for the 3 min interval with these inconsistent phase delays is very low ($\gamma = 0.1$) at the peak of PSD_$\delta b_{xy}$. However, the degree of polarization is 0.9 at the peak frequency with the ellipticity of 0.05. This high degree of polarization is due to the large-amplitude difference between $\delta b_x$ and $\delta b_y$ oscillations. Since the relative phase variations occur randomly, it is impossible to obtain meaningful ellipticity at the peak of PSD_$\delta b_{xy}$ even though $R$ is large.

The incoherent phase delays between $\delta b_x$ and $\delta b_y$ occurred more frequently in the 3 min interval of 16:01–16:04 UT shown in Figure 5f. The amplitude of the two field components is comparable. The relative phase between $\delta b_x$ and $\delta b_y$ changes rapidly and randomly within a few cycles. For example, the oscillations starting around 16:03 UT are seen with similar amplitude and wave packet in $\delta b_x$ and $\delta b_y$, but their periods are different. The $\delta b_x$ and $\delta b_y$ oscillations were initially in phase and then gradually became out of phase after two cycles. On detailed examination of the waveforms of $\delta b_x$ and $\delta b_y$, we found that the period of $\delta b_y$ is significantly shorter than that of $\delta b_x$, notably at ~16:02:30 UT, and the $\delta b_y$ wave train contains some phase skips.

In the frequency domain, the above results can be confirmed. The spectral shapes of $\delta b_x$ and $\delta b_y$ shown in Figure 5g significantly differ in the enhanced frequency band of 100–400 mHz. The $\delta b_y$ spectrum is much broader than the $\delta b_x$ spectrum. The $\delta b_y$ spectrum is peaked at ~240 mHz, while the $\delta b_x$ spectrum is peaked at ~210 mHz. The coherence is peaked ($\gamma = 0.72$) at ~267 mHz, slightly higher than the peak of $\delta b_y$, and rapidly decreases to 0.13 at the spectral peak of $\delta b_y$. That is, the coherence is not consistently high in the enhanced frequency band. The $\delta b_y$ power is larger than the $\delta b_x$ power by a factor of ~6 at the $\delta b_y$ spectral
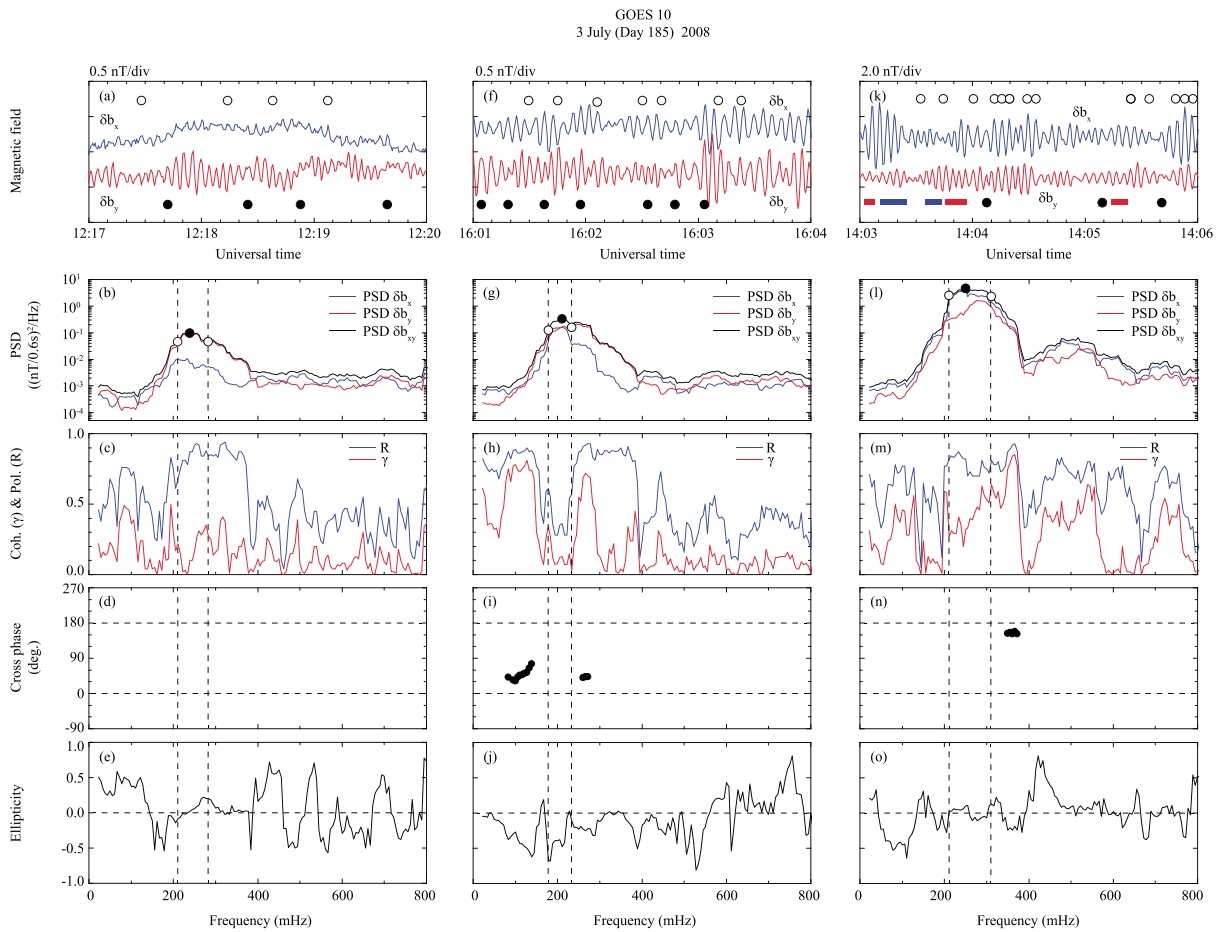
**Figure 5.** The low-coherence time series of the transverse components and spectral properties for two 3 min intervals, 12:17–12:20 UT, 14:03–14:06 UT, and 16:01–16:04 UT on 3 July 2008, in the same format as for Figure 4. In-phase oscillations are marked by solid circles, and out of phase oscillations are marked by open circles. The red (blue) horizontal bar in Figure 5k indicates the interval when $\delta b_y$ ($\delta b_x$) leads $\delta b_x$ ($\delta b_y$).

peak, while both powers are nearly identical at the $\delta b_x$ spectral peak. The total transverse power, PSD_$\delta b_{xy}$, exhibits a peak at the same frequency as the $\delta b_x$ spectral peak. These spectral signatures indicate that $\delta b_y$ contains more various waves. The coherence and degree of polarization calculated for the 3 min interval are very low ($\gamma = 0.13$ and $R = 0.36$) at the peak frequency of PSD_$\delta b_{xy}$, indicating that the EMIC waves are highly unpolarized.

Figure 5k shows the transverse magnetic field data for a 3 min interval (from 14:03 to 14:06 UT) of strongly enhanced EMIC wave pulsations (see Figure 3). Note that the scale for the amplitude of the oscillations in Figure 5k is different from that in Figures 5a and 5f. The red (blue) horizontal bar indicates the interval when $\delta b_y$ ($\delta b_x$) leads $\delta b_x$ ($\delta b_y$). $\delta b_x$ and $\delta b_y$ oscillated out of phase for two and three cycles. That is, the constant phase between $\delta b_x$ and $\delta b_y$ lasted only a few wave cycles of data. The relative phase and amplitude of the two components change rapidly although their periods are similar. As expected, the $\delta b_x$-$\delta b_y$ coherence at the enhanced frequency band is low, which means that we cannot find any meaningful ellipticity for the oscillations in the frequency band.

Since the spectral peaks of $\delta b_x$ and $\delta b_y$ do not always appear at the same frequency, we use the spectral parameters (the coherence, degree of polarization, and ellipticity) averaged over the frequency band ($\Delta f$) between $f_{lower}$ and $f_{upper}$, which is occupied by the spectral peak of PSD_$\delta b_{xy}$, in the statistical study presented below. The EMIC wave power ($P_{tr}$) in P1 was obtained by integrating PSD_$\delta b_{xy}$ over the local He-band frequency range. In this study, however, $P_{tr}$ is defined as the integral of PSD_$\delta b_{xy}$ over $\Delta f$ because we do not limit EMIC waves to the He band, although GOES data do not provided spectral parameters over the entire H band at geosynchronous orbit on the dayside [Fraser et al., 2012; Clausen et al., 2011]. Once the $P_{tr}$ peaks are determined, they are plotted in the format of frequency and universal time (UT) and verified
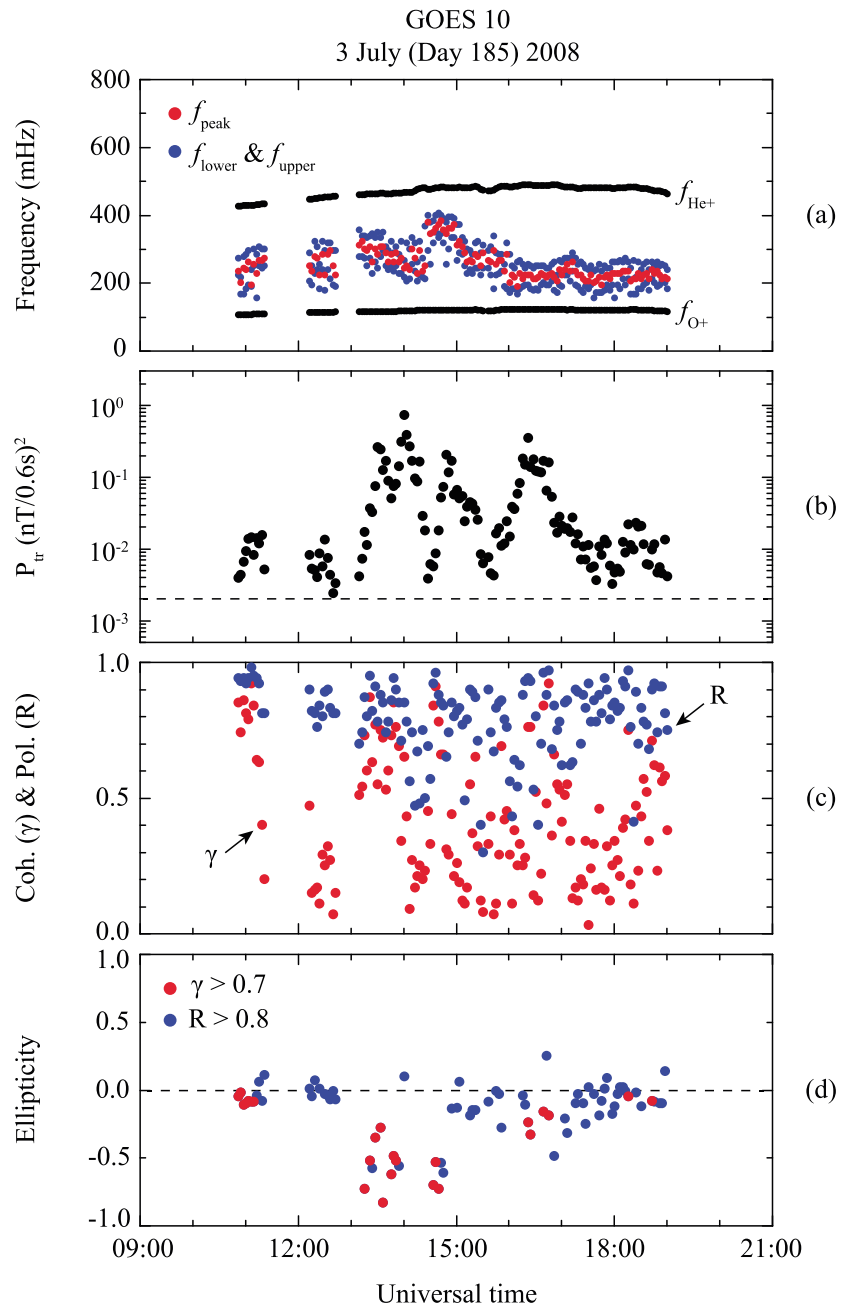
**Figure 6.** The spectral parameters of the EMIC wave samples for the same interval shown in Figure 3. (a) The spectral peak (marked by a red circle, $f_{peak}$) of EMIC wave power ($P_{tr}$) and its width (marked by blue circles, $f_{lower}$ and $f_{upper}$). (b) $P_{tr}$. (c) coherence (red dots) and degree of polarization (blue dots). (d) Ellipticity. Red (blue) dots in ellipticity indicate the high coherence (degree of polarization) samples.

by manually comparing them against the 24 h dynamic spectra of the format shown in Figure 3. This semiautomated EMIC wave selection procedure was also used in P1. We impose the power threshold of 0.002 $(nT/0.6\,s)^2$ in event selection. Throughout this paper we adopt a 3 min time window (180 data points at 0.6 s time resolution) to obtain the spectral parameters of EMIC waves. The parameters are calculated in nonoverlapping 3 min segments.

Figure 6 shows the spectral parameters of the EMIC wave samples, obtained by the moving time window analysis, for the same interval shown in Figure 3. We identified 139 $P_{tr}$ samples by the semiautomated procedure for the 12 h interval. There are gaps for the intervals, 11:22–12:13 UT and 12:43–13:10 UT.
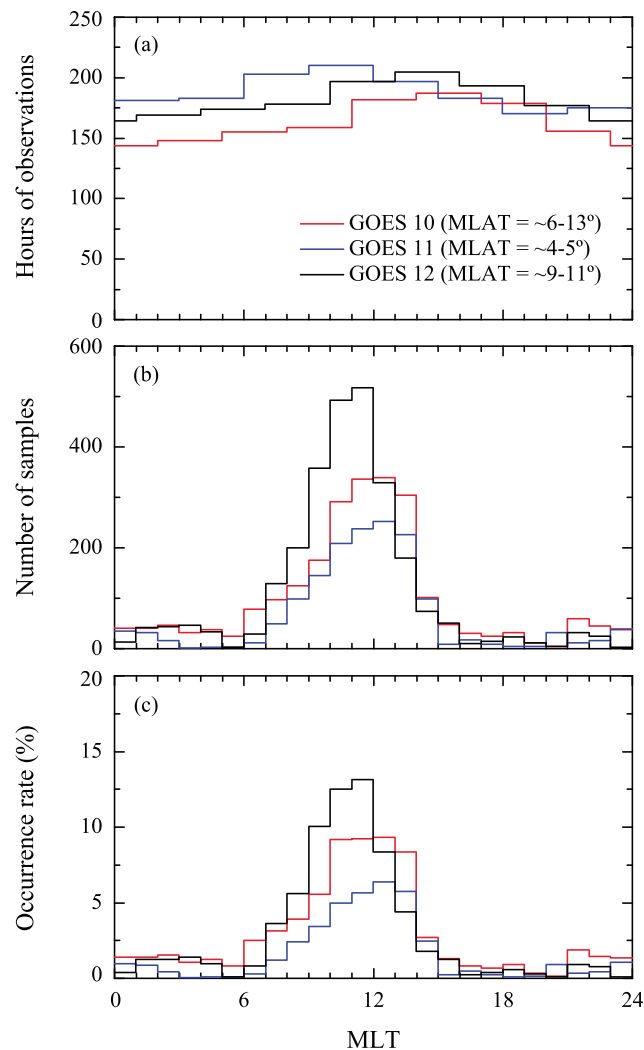
**Figure 7.** (a) The distribution of the total observation time with MLT under steady quiet conditions for three GOES satellites. (b) The local time distribution of the $P_{tr}$ samples. (c) The occurrence rate of EMIC wave samples at each spacecraft. The occurrence rate was calculated by dividing the net observation time of samples by total observation time for each 1 h MLT bin.

These are caused by the threshold imposed on $P_{tr}$. Spectral peak frequencies (red circles) and $\Delta f$ for each peak (blue circles) are plotted with $f_{He^+}$ and $f_{O^+}$ in Figure 6a. Comparing with the dynamic spectra in Figure 3, we confirm that the peak frequency and $\Delta f$ well indicate the frequency band, in which the EMIC waves are enhanced. Figures 6b–6d show $P_{tr}$, coherence, degree of polarization, and ellipticity, respectively. Of the 139 samples, 24 (~17%) samples show high coherence ($\gamma > 0.7$), and 80 (~58%) samples show high degree of polarization ($R > 0.8$). As expected in Figure 3, there are many high-polarization samples with low coherence. The ellipticity parameters are plotted only for $\gamma > 0.7$ (red circles) and $R > 0.8$ (blue circles) in Figure 6d. The ellipticity indicates that EMIC waves with the high $\gamma$ and $R$ values are linearly and left-hand polarized.

## 4. Statistical Analysis

### 4.1. MLT and MLAT Dependence of Quiet-Time EMIC Wave Detection Rate

Using the semiautomated EMIC wave selection procedure, we identify 2364 $P_{tr}$ samples at GOES 10 located at 60°W geographic longitude and slightly off the equator (MLAT (magnetic latitude) ~ 6–13°), 1556 samples at GOES 11 at 135°W near the magnetic equator (MLAT ~ 4–5°), and 2664 samples at GOES 12 at 75°W and slightly off the equator (MLAT ~ 9–11°), respectively, during quiet-time intervals ($Kp \leq 1$) following steady
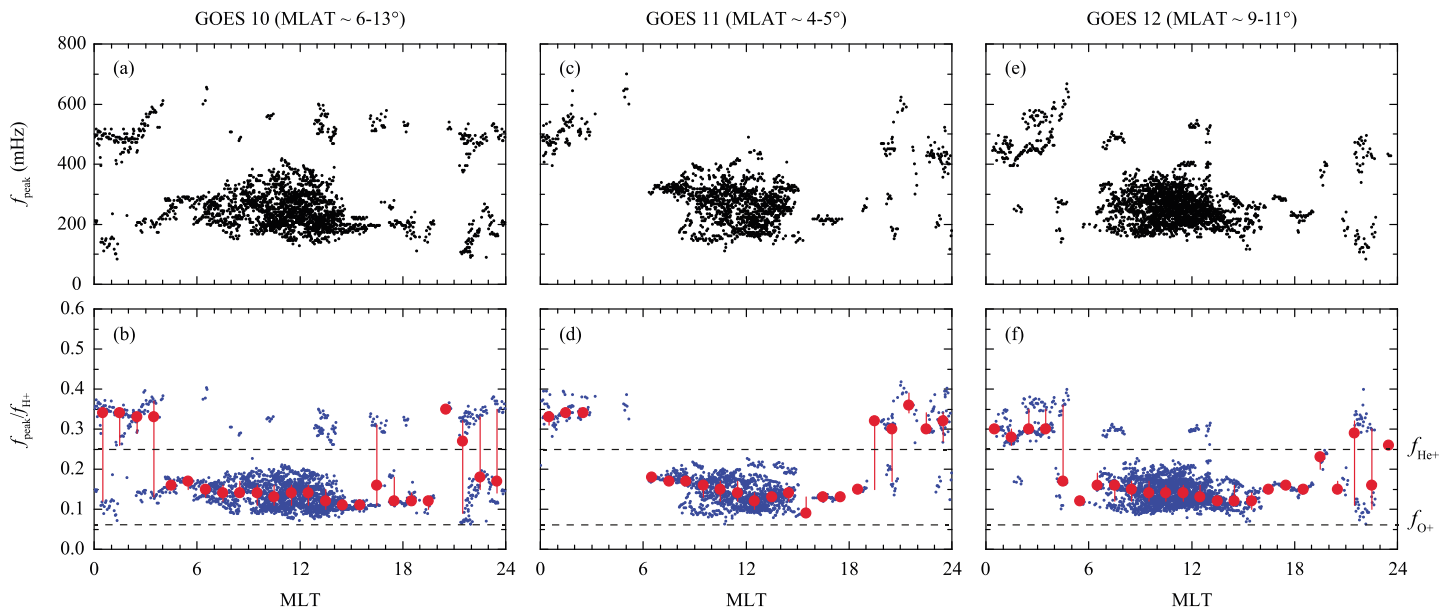
**Figure 8.** Scatterplots of $f_{peak}$ and $f_{peak}/f_{H^+}$ as a function of MLT at GOES spacecraft. The small dots indicate individual samples, the large red dots connected by a straight line indicate the medians in the MLT bins, and the vertical bars connect the lower and upper quartiles. There is a tendency for the medians of $f_{peak}/f_{H^+}$ over ~0600−1500 MLT to decrease monotonically from morning to afternoon.

quiet conditions in 2007−2008. The MLAT is computed based on an Earth center dipole. Since GOES satellites were located at different latitudes and longitudes, we examine whether the different number of samples is caused by sampling bias at each geosynchronous spacecraft.

Figure 7a shows the distribution of the total observation time with MLT under steady quiet conditions. The distribution in MLT at each satellite is slightly biased: there are more observations in the prenoon sector at GOES 11 and in the postnoon sector at GOES 10 and GOES 12. Figures 7b and 7c show the local time distribution of the $P_{tr}$ samples (or 3 min intervals) and the occurrence rate at each spacecraft. The occurrence rate was calculated by dividing the net observation time of samples by total observation time for each 1 h MLT bin. The majority of the samples were observed in the morning-to-early afternoon sector (~0700−1500 MLT) with a peak occurrence near noon, which is consistent with P1 because our samples are the subset of quiet-time EMIC waves identified in P1. In addition, Figure 7 gives further information for the latitudinal occurrence distribution. Comparing the occurrence rates at GOES 11 near the equator (MLAT ~ 4−5°) and GOES 12 off the equator (MLAT ~ 9−11°), the occurrence rate off the equator is higher than near the equator, indicating that EMIC waves are more frequently detected off the equator. This result is consistent with previous study [*Fraser*, 1985].
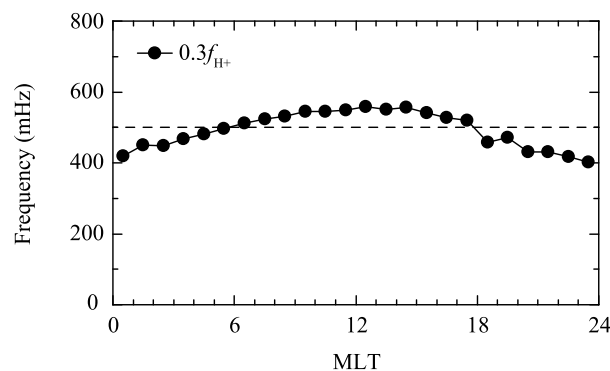


**Figure 9.** The hourly medians of $0.3f_{H^+}$ for the samples, calculated with magnetic fields observed from three GOES spacecraft. The dashed horizontal line indicates the 500 mHz cutoff frequency.
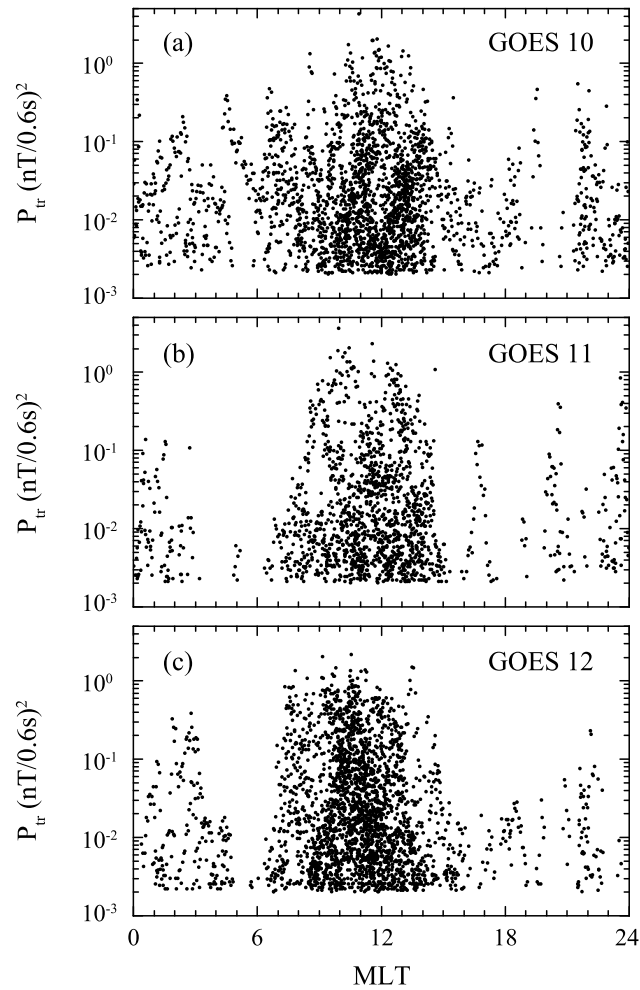
**Figure 10.** $P_{tr}$-MLT scatterplots at three GOES spacecraft. Since the $P_{tr}$ samples are highly scattered at each local time, leading to a large uncertainty, median statistics for the samples are not made.

### 4.2. Spectral Characteristics of Quiet-Time EMIC Waves

Figure 8 shows a scatterplot of $f_{peak}$ and $f_{peak}/f_{H^+}$ ($f_{peak}$ normalized to the local proton gyrofrequency frequency) as a function of MLT at GOES spacecraft. The small dots indicate individual samples, the large dots connected by a straight line indicate the medians in the MLT bins, and the vertical bars connect the lower and upper quartiles. The median values are displayed only in MLT bins containing more than five samples. In the $f_{peak}/f_{H^+}$ plots, the horizontal dashed lines indicate the helium and oxygen gyrofrequencies, respectively. Since the samples appear in the He band and/or in the H band, the arithmetic mean is sensitive to a small number of samples that have large values of $f_{peak}/f_{H^+}$ in the H band. Thus, we use median values instead of mean values for statistical analysis. The large error bars in premidnigh and postmidnigh are due to the appearance of EMIC waves in both He and H bands. The $f_{peak}$ plots show a strong concentration of data points in the frequency band of ∼150–400 mHz in the 0600–1500 MLT sector. They are lying between $f_{O^+}$ and $f_{He^+}$, indicating that the majority of steady quiet-time EMIC waves occur in the He band, as observed in the example shown in Figures 3 and 6. In the remainder of the MLT, the small number of samples appears in the He and H bands. These results are similar to CRRES observations over radial rage $L = ∼ 4–7$ [*Fraser and Nguyen*, 2001; *Meredith et al.*, 2014]. The medians in the He band at three GOES spacecraft lie in the range of $f_{peak}/f_{H^+} = ∼ 0.11–0.16$ over ∼0600–1500 MLT where the majority of the He-band EMIC waves occur. There is a tendency for the medians in that local time sector to decrease monotonically from morning to afternoon. The mean values show the same trend as the medians and are in the range between 0.12 and 0.16 over the local time sector (data not shown).
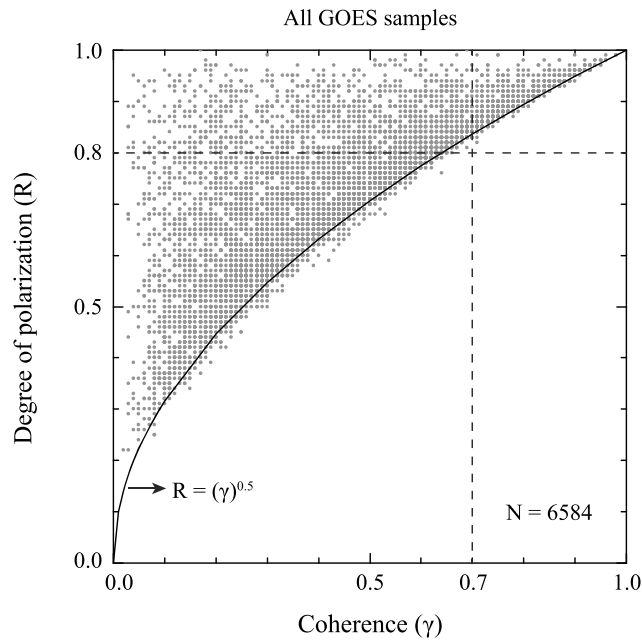
**Figure 11.** Scatterplot of degree of polarization ($R$) versus coherence ($\gamma$) for all GOES $P_{tr}$ samples. The solid curve indicates $R = (\gamma)^{0.5}$. Most samples lie above the solid curve corresponding to $R = (\gamma)^{0.5}$.

It should be noted that our observations for EMIC wave activities in the H band might result from nongeophysical effect. As pointed out by *Clausen et al.* [2011] and *Fraser et al.* [2012], the GOES magnetic field data were filtered through a five-pole Butterworth low-pass filter in the frequency band of 0.5–1 Hz. The response in that band is reduced by the low-pass filter, and thus, the EMIC wave events in the H band above 500 mHz would
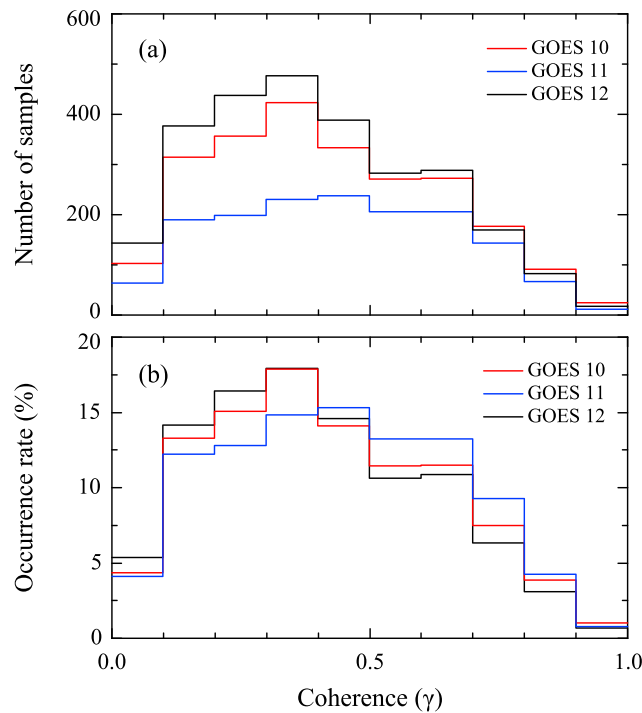


**Figure 12.** (a) Occurrence frequency distribution of $P_{tr}$ samples for coherence values. (b) The occurrence rate obtained by dividing the number of the $P_{tr}$ sample in each 0.1-coherence bin by total number of samples. Higher coherence samples ($\gamma > 0.5$) are more frequently detected near the equator.
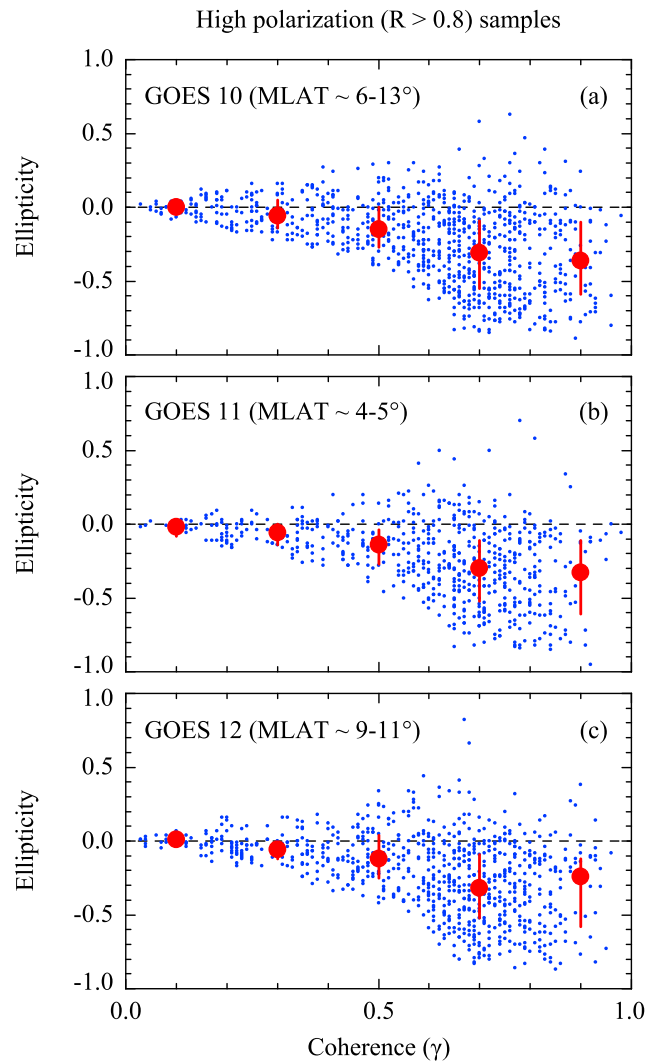
High polarization (R > 0.8) samples



**Figure 13.** Scatterplot of ellipticity versus coherence for the high-polarization ($R > 0.8$) samples at (a) GOES 10, (b) GOES 11, and (c) GOES 12. In each panel the small dots (blue) are individual samples, the large dots (red) are the medians within each 0.2-coherence bin, and the vertical bars connect the lower and upper quartiles. The degree of the data scatter increases as $\gamma$ increases.

be missed. In previous study [*Anderson et al.*, 1992b], AMPTE/CCE observations reported that the dayside EMIC waves near geosynchronous orbit ($L = 6-7$) occur mainly in the H band with $f_{peak}/f_{H^+} = \sim 0.3-0.4$. Assuming $f_{peak}/f_{H^+} = 0.3$, we examine the MLT dependence of lower frequencies for EMIC waves in the H band with respect to the cutoff frequency of 500 mHz. Figure 9 shows the hourly medians of $0.3f_{H^+}$ for the samples, calculated with magnetic fields observed from three GOES spacecraft, with the 500 mHz cutoff frequency (dashed horizontal line). In the dayside the frequencies of $0.3f_{H^+}$ are above 500 mHz, while their frequencies are below 500 mHz in the premidnight and postmidnight sectors. Thus, we do not exclude the possibility that the H band EMIC waves appearing and disappearing along the local time are due to the filtering effect.

Figure 10 shows the $P_{tr}$-MLT scatterplots at three GOES spacecraft. Since the $P_{tr}$ samples are highly scattered at each local time, leading to a large uncertainty, we do not make median statistics for the samples. $P_{tr}$ varies $\sim 2-3$ orders of magnitude, ranging from 0.002, which is the threshold value for $P_{tr}$, to greater than 1 (nT/0.6 s)$^2$. This indicates that EMIC wave power varies from event to event, as shown in the example (Figures 3 and 6), even under quiet geomagnetic conditions. Significant EMIC waves with $P_{tr} > 0.1$ (nT/0.6 s)$^2$ were mostly observed in the region where the majority of the He-band waves occur. Recently, *Hyun et al.* [2014] and P1 reported that the He-band EMIC waves with power greater than 0.1 (nT/0.6 s)$^2$ can be excited by small enhancements in solar wind dynamic pressure under quiet conditions.
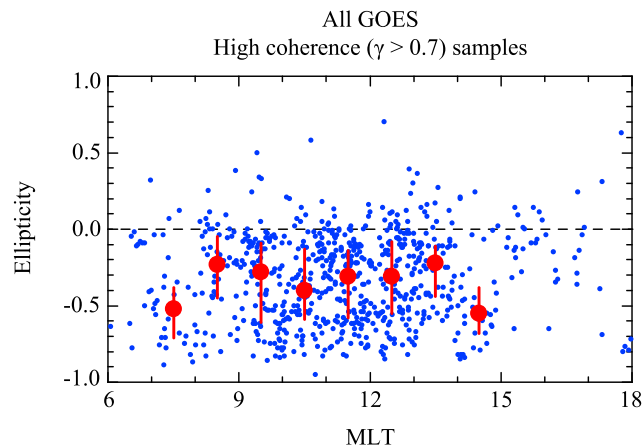
**Figure 14.** The ellipticity for high-coherence ($\gamma > 0.7$) samples over 0600–1800 MLT as a function of MLT. The median values with error bars are displayed only for 0700–1500 MLT, where the majority of the He-band EMIC waves were detected. The median values are distributed in the range of $-0.5$ to $-0.2$ without local time dependence.

Figure 11 shows the relationship between coherence and degree of polarization for all GOES $P_{tr}$ samples. The vertical and horizontal dashed lines indicate $\gamma = 0.7$ and $R = 0.8$, respectively. Most samples lie above the solid curve corresponding to $R = (\gamma)^{0.5}$. Out of 6584 samples, 2288 (~35%) samples show high polarization ($R > 0.8$). However, they are distributed over a wide range of $\gamma$ between 0 and 1, and only 783 (~34%) samples of these high $R$ samples exceed $\gamma = 0.7$. That is, ~12% of total samples have high coherence between $\delta b_x$ and $\delta b_y$. This indicates that meaningful polarization properties can be obtained from only a small fraction of steady quiet-time EMIC waves observed at geosynchronous orbit.

In order to examine whether there is the MLAT dependence of high-coherence samples, we computed the occurrence rate for three GOES satellites, which were located at different latitudes. The result is shown in Figure 12. The occurrence rate is obtained by dividing the number of the $P_{tr}$ sample in each 0.1-coherence bin by total number of samples. By comparing the occurrence rates at GOES 11 (near the equator, MLAT = ~4–5°) and GOES 12 (off the equator, MLAT = ~9–11°), we found that the occurrence rate of the samples for $\gamma = 0.5$–0.9 at GOES 11 is about 1–3% higher than that at GOES 12. That is, the overall occurrence rate of higher coherence samples ($\gamma > 0.5$) is higher near the equator, implying that more coherent EMIC waves appear near the equator.

Figure 13 shows a scatterplot of ellipticity versus coherence for the high-polarization ($R > 0.8$) samples. In each panel the small dots (blue) are individual samples, the large dots (red) are the medians within each 0.2-coherence bin, and the vertical bars connect the lower and upper quartiles. The distribution of the ellipticity exhibits no significant difference among GOES satellites. It is clear that the degree of the data scatter increases as $\gamma$ increases. Most samples with $\gamma < 0.3$ are scattered around zero, indicating linearly polarized, with a small spread of data points. Since the coherence is very low for the samples, reliable polarization results cannot be obtained from them even though $R > 0.8$. Thus, the linear polarized waves are required to examine whether the relative phase variations of the oscillations in $\delta b_x$ and $\delta b_y$ are coherent. Ellipticity for the high-coherence ($\gamma > 0.7$) samples is distributed between $-0.8$ and $0.2$, indicating left-handed and linear polarization, with median values around $-0.3$.

The ellipticity for high-coherence ($\gamma > 0.7$) samples over 0600–1800 MLT is plotted as a function of MLT in Figure 14. The median values with error bars are displayed only for 0700–1500 MLT, where the majority of the He-band EMIC waves were detected. As expected from Figure 13, most of samples are below zero, and the median values are distributed in the range of $-0.5$ to $-0.2$ without local time dependence. This result is similar to previous observations from AMPTE/CCE and CRRES satellites for the He-band EMIC waves [*Anderson et al.*, 1992b; *Fraser and Nguyen*, 2001].
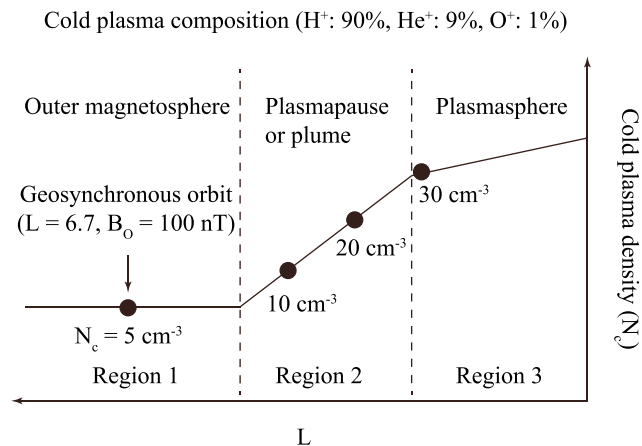
Cold plasma composition (H$^+$: 90%, He$^+$: 9%, O$^+$: 1%)



**Figure 15.** Schematic illustration of radial cold plasma density ($N_c$) distribution. See the text for descriptions.

## 5. Discussion

### 5.1. Comparison With Previous Observations

The occurrence rate of steady quiet-time EMIC waves observed at geosynchronous orbit is higher than 5% in the morning-to-early afternoon sector (0700–1500 MLT). The peak occurrence rate near noon is ~13% at GOES 12, ~9% at GOES 10, and ~6% at GOES 11, respectively. These rates are much greater than previous AMPTE/CCE and THEMIS observations on the dayside. THEMIS observations showed that the occurrence rate of dayside (0900–1500 MLT) EMIC waves without distinguishing in the He and H bands is lower than 3% near geosynchronous orbit under quiet geomagnetic activities [*Usanova et al.*, 2012]. AMPTE/CCE observations using ~4.5 year data reported that the He-band event occurrence rate near the morning-to-afternoon sector is lower than 5% under quiet geomagnetic conditions [*Keika et al.*, 2013].

It is generally accepted that the source region of EMIC waves is near the equator and extended to ±11° in magnetic latitude [*Fraser et al.*, 1996; *Loto'aniu et al.*, 2005]. Although GOES satellites observed EMIC waves near the source region, there is a MLAT dependence of the rate. That is, the occurrence rate near the equator (GOES 11, MLAT ~ 4–5°) is lower than off the equator (GOES 10, MLAT ~ 6-13° and GOES 12, MLAT ~ 9–11°) as shown in Figure 7. Considering that the EMIC wave growth can maximize in the region where the magnetic field strength is minimum [e.g., *Cornwall*, 1965; *Kennel and Petschek*, 1966], GOES 11 is well inside the source region and closely located to the region favored for EMIC wave generation, while GOES 12 was near the upper boundary of the source region. We suggest that GOES 11 near the equator mainly observes EMIC waves generated in the source region rather than waves propagating from the source region, while GOES 12 off the equator observes both generated and propagating waves. Thus, EMIC waves are more frequently detected at GOES 12 than at GOES 11. The occurrence rate at GOES 10 is between the values at GOES 11 and GOES 12. This may be due to the fact that GOES 10 was just inside or outside the source region.

Our observations showed that the medians and means of $f_{peak}/f_{H^+}$ are in the range of ~0.11–0.16 and ~0.12–0.16, respectively, in the morning-to-afternoon sector (0700–1500 MLT) where the majority of the He-band EMIC waves occur. In a previous study using the 1 year data set in 2007 of GOES 11 and GOES 12 for the all-*Kp* case, the mean values of $f_{peak}/f_{H^+}$ are distributed in the range of ~0.14–0.24 over the same local time sector [*Fraser et al.*, 2012]. This indicates that frequencies of He-band EMIC waves under steady quiet conditions shift toward lower frequency close to the oxygen gyrofrequency.

### 5.2. EMIC Wave Occurrence and Cold Plasma Density

The relatively high occurrence rate of the He-band waves in our study may be explained in terms of cold plasma distribution under quiet geomagnetic conditions. It has been known that the EMIC wave growth can be enhanced by increasing the cold background plasma density [e.g., *Cornwall et al.*, 1970; *Kozyra et al.*, 1984; *Horne and Thorne*, 1994; *Hu and Fraser*, 1994]. The plasmapause is a preferred region for the generation of EMIC waves [e.g., *LaBelle et al.*, 1988; *Fraser et al.*, 1989; *Kim et al.*, 2016] even though highest occurrence rate is in the outer magnetosphere (*L* > 7) [e.g., *Anderson et al.*, 1992a; *Min et al.*, 2012; *Usanova et al.*, 2012; *Keika et al.*, 2013].
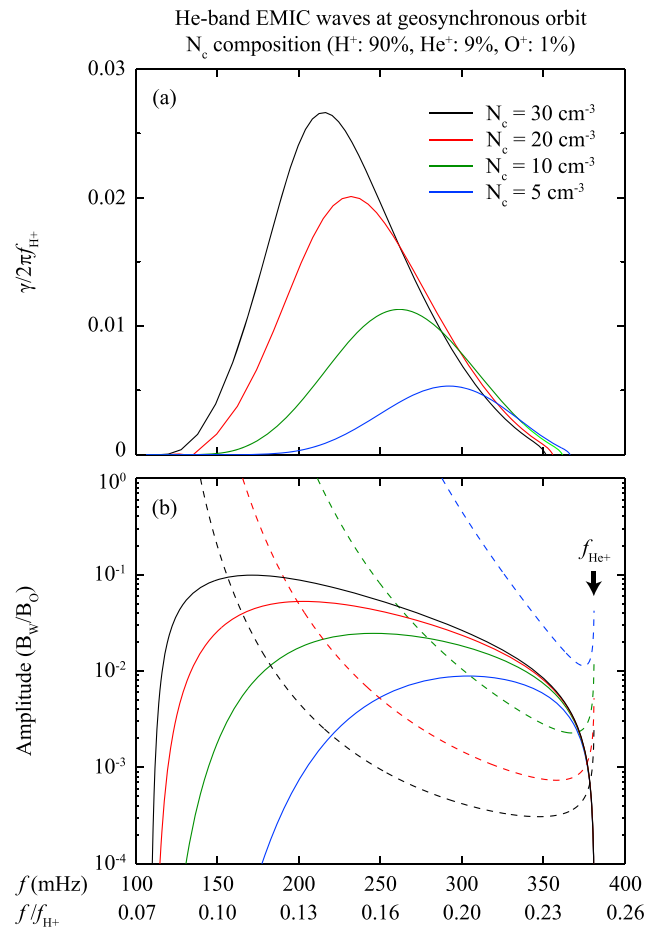
**Figure 16.** (a) Linear growth rate of EMIC waves as a function of frequency and normalized frequency at geosynchronous orbit for $N_c = 5$ cm$^{-3}$ (blue), 10 cm$^{-3}$ (green), 20 cm$^{-3}$ (red), and 30 cm$^{-3}$ (black), which are marked by solid dots in Figure 15. (b) Optimum amplitudes (solid lines) and threshold amplitudes (dashed lines) of nonlinear growth for $N_c = 5$ cm$^{-3}$, 10 cm$^{-3}$, 20 cm$^{-3}$, and 30 cm$^{-3}$.

The plasmapause is located around $L = 4$–5 under moderate geomagnetic conditions, but if the magnetosphere is quiet, the plasmapause expands to the geosynchronous region or beyond. Recently, *Kwon et al.* [2015] reported that the plasmapause is often identified beyond geosynchronous orbit with the average plasmapause location near geosynchronous orbit under steady quiet geomagnetic conditions. Our EMIC wave samples are taken from the period of 2007–2008 in a solar minimum, and about 50% of this period were under quiet geomagnetic conditions ($Kp \leq 1$) as noted in P1. Thus, the geosynchronous region is more often to be a region for EMIC wave generation in the 2007–2008 period than other periods selected in previous studies.

In order to examine the effect of cold plasmas on EMIC waves observed at geosynchronous orbit, we assume a radial cold plasma density distribution plotted in Figure 15. At geosynchronous orbit in the outer magnetosphere (region 1), the background magnetic field ($B_o$) and cold plasma density ($N_c$) are assumed to be 100 nT and 5 cm$^{-3}$, respectively. In the plasmasphere (region 3), $N_c$ just inside the plasmapause (i.e., at inner boundary of the plasmapause) is assumed to be 30 cm$^{-3}$. This cold plasma density is not the value at the plasmapause normally located at $L = 4$–5 but at the plasmapause expanded to or beyond geosynchronous orbit [*Kwon et al.*, 2015]. The plasma density between 5 and 30 cm$^{-3}$ in region 2 indicates the value of the density gradient region corresponding to the plasmapause or in the plasmaspheric plume [e.g., *McFadden et al.*, 2008]. The cold ion composition is assumed to be 90% H$^+$, 9% He$^+$, and 1% O$^+$.

Figure 16a shows the linear growth rate as a function of frequency and normalized frequency at geosynchronous orbit for $N_c = 5$ cm$^{-3}$, 10 cm$^{-3}$, 20 cm$^{-3}$, and 30 cm$^{-3}$, which are marked by solid dots in Figure 15. The growth rate presented in this study was calculated by using the Kyoto University Plasma Dispersion
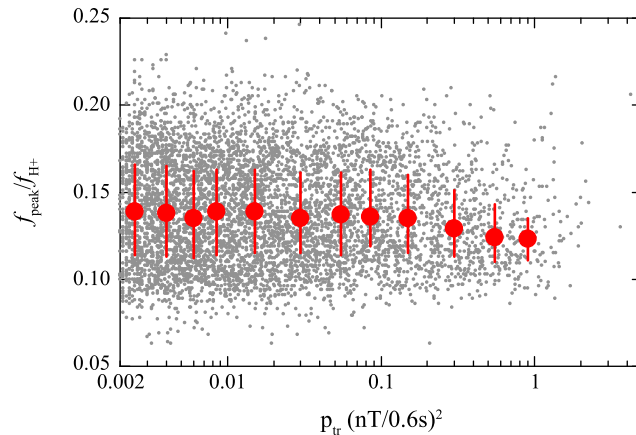
**Figure 17.** Scatterplot of $f_{peak}/f_{H^+}$ versus He-band $P_{tr}$. The large red dots are medians in logarithmically spaced $P_{tr}$ bins. The vertical bars connect the lower and upper quartiles in the $P_{tr}$ bin. The median value goes down to $\sim 0.12$ for $P_{tr} > 0.2$.

Analysis Package (KUPDAP), which is a dispersion solver developed by the Space Group at Kyoto University, Kyoto, Japan [*Sugiyama et al.*, 2015]. In KUPDAP energetic proton populations are considered to be $T_\perp/T_\parallel = 1.7$, the kinetic energy of 33 keV, and 4.5% of the total proton population. The maximum growth rate appears at 293 mHz for $N_c = 5$ cm$^{-3}$ (blue), 261 mHz for $N_c = 10$ cm$^{-3}$ (green), 232 mHz for $N_c = 20$ cm$^{-3}$ (red), and 215 mHz for $N_c = 30$ cm$^{-3}$ (black), respectively. Those frequencies are well in the frequency range of the He-band EMIC waves observed in the morning-to-early afternoon sector (0700–1500 MLT) (see Figure 8). In Figure 16a we confirm that wave growth increases with increasing $N_c$ and that the peak in the growth rate shifts toward lower frequencies as geosynchronous orbit encounters the increasing $N_c$.

The optimum amplitudes (solid lines) and threshold amplitudes (dashed lines) for the nonlinear wave growth are plotted for the four $N_c$ values in Figure 16b. Detailed theoretical descriptions for the optimum and threshold amplitudes for the nonlinear wave growth are provided in *Omura et al.* [2010] and *Shoji and Omura* [2013]. Since the wave amplitudes for $N_c = 5$ cm$^{-3}$ are below the threshold amplitude, EMIC-triggered emissions do not occur. This does not mean that the waves are not generated in a source region but that waves are strongly localized in a generation region without growing. It is clear that the frequency range of the optimum amplitude above the threshold increases as $N_c$ increases and that wave power increases as frequency decreases in the frequency range.

In order to compare theoretical predictions for nonlinear wave growth and observations, we plot $f_{peak}/f_{H^+}$ versus He-band $P_{tr}$ in Figure 17. As expected in Figure 8, $f_{peak}/f_{H^+}$ is mostly in the range between 0.1 and 0.2. The distribution of $f_{peak}/f_{H^+}$ is comparable to the frequency range of the optimum amplitude above the threshold for $N_c = 20$ and 30 cm$^{-3}$. Thus, we suggest that EMIC waves observed at geosynchronous orbit under steady quiet conditions may be generated in the dense plasmaspheric plasma. There is no clear $P_{tr}$ dependence of $f_{peak}/f_{H^+}$ from $P_{tr} = 0.002$ and $P_{tr} = 0.2$. That is, the medians are staying at $f_{peak}/f_{H^+} = \sim 0.14$. However, the median value goes down to $\sim 0.12$ for $P_{tr} > 0.2$. This is qualitatively consistent with higher power EMIC waves at lower frequencies shown in Figure 16b.

We observed that the $f_{peak}/f_{H^+}$ median values change with local time over in the morning-to-afternoon sector ($\sim 0700–1500$ MLT). That is, the values are higher in the morning and lower in the afternoon. Most recently, Kim et al. (Occurrence of EMIC waves and plasmaspheric plasmas derived from THEMIS observations in the outer magnetosphere: Revisit, submitted to *Journal of Geophysical Research*: *Space Physics*, 2016) reported that there is a morning-afternoon asymmetry of plasmaspheric plasma density in the outer magnetosphere under quiet geomagnetic conditions ($Kp \leq 1$). Higher plasmspheric density is observed in the afternoon sector. The decreasing $f_{peak}/f_{H^+}$ values with local time might be explained with a asymmetric local time signature of plasmaspheric density distribution.

### 5.3. Coherence Between $\delta b_x$ and $\delta b_y$

In our statistical result we showed that only $\sim 12\%$ of total samples showed high coherence between $\delta b_x$ and $\delta b_y$ components, implying that a large fraction of EMIC waves observed at GOES satellites are phase incoherent between the transverse components. The theory of wave-particle interactions with EMIC waves describes

that EMIC waves play an important role in the loss of relativistic electrons in the Earth's radiation belts into the Earth's atmosphere [e.g., *Horne*, 2002; *Summers and Thorne*, 2003; *Shprits et al.*, 2006, 2013; *Usanova et al.*, 2014], and it has been used to explain precipitation of relativistic electrons observed at low-altitude polar-orbiting spacecraft [e.g., *Miyoshi et al.*, 2008; *Rodger et al.*, 2010; *Yuan et al.*, 2012; *Hyun et al.*, 2014]. It has been reported that the efficiency of the pitch-angle scattering for relativistic electrons interacting with coherent EMIC waves depends on the gradient of the magnetic field, the frequency sweep rate, and the wave amplitude [*Omura and Zhao*, 2012]. This indicates that only a small fraction of EMIC waves observed in space contributes to the pitch-angle scattering.

The lack of $\delta b_x$-$\delta b_y$ coherence is caused by the fact that the phase of two signals varies randomly for several cycles, like the example shown in Figure 5. If a satellite is in the generation region of EMIC waves and detects only newly generated waves, phase-coherent sinusoidal waves can be expected in the $\delta b_x$ and $\delta b_y$ waveforms. However, if a satellite observes propagating and generated waves near the source region, long-lasting wave matching in period and phase between the two components cannot be found because the observed waves consist of various waves with slightly different frequencies and wavelengths. With this argument we can explain why more coherent EMIC waves exist near the equator than off the equator as shown in Figure 12.

## 6. Conclusion

We have examined the spectral characteristics of steady quiet-time EMIC waves observed at geosynchronous orbit for the solar minimum years 2007–2008. Most of EMIC waves appear in the He band and are distributed in the morning-to-early afternoon sector (∼0700–1500 MLT). The EMIC wave occurrence rate in our study is higher than that in previous studies by a factor of 2 or more. The peak occurrence rate near noon is ∼13% at GOES 12, ∼9% at GOES 10, and ∼6% at GOES 11, respectively. The relatively high wave occurrence probably results from the expansion of the plasmasphere to geosynchronous orbit under extremely quiet geomagnetic conditions in 2007–2008.

We examined the effect of cold plasmas on EMIC wave generation and showed that maximum growth rate of EMIC wave in the He-band shifts to lower frequency as the cold background plasma density increases. As mentioned above, geosynchronous satellites presumedly experience frequent appearance of dense plasmaspheric plasma under steady quiet conditions. The frequency ratio $f_{peak}/f_{H^+}$ of the quiet-time He-band waves is ∼0.11–0.16, which is lower than that (∼0.14–0.24) in previous study. We interpret the lower values of $f_{peak}/f_{H^+}$ in our study as a consequence of plasmasphere expansion to the geosynchronous region. The amplitude and frequency of He-band EMIC waves for nonlinear wave growth are examined as changing cold plasma density at geosynchronous orbit. We confirmed that the spectral properties of observed EMIC waves are in good agreement with the nonlinear theory.

We observed that only ∼12% of EMIC wave samples have high coherence (>0.7) between the two transverse components, $\delta b_x$ and $\delta b_y$. Since the source region has been considered to be located near the equator within ±11° MLAT, the observed fluctuations at GOES satellites consist of various waves, which are generated with different growth histories. Thus, their frequencies and wavelengths might be slightly different. These waves will interfere in a complicated manner as they propagate from the source and will show phase-incoherent signatures between $\delta b_x$ and $\delta b_y$.

## References

Anderson, B. J., R. E. Erlandson, and L. J. Zanetti (1992a), A statistical study of Pc 1-2 magnetic pulsations in the equatorial magnetosphere: 1. Equatorial occurrence distributions, *J. Geophys. Res.*, *97*(A3), 3075–3088, doi:10.1029/91JA02706.

Anderson, B. J., R. E. Erlandson, and L. J. Zanetti (1992b), A statistical study of Pc 1-2 magnetic pulsations in the equatorial magnetosphere: 2. Wave properties, *J. Geophys. Res.*, *97*(A3), 3089–3101, doi:10.1029/91JA02697.

Anderson, B. J., and D. C. Hamilton (1993), Electromagnetic ion cyclotron waves stimulated by modest magnetospheric compressions, *J. Geophys. Res.*, *98*(A7), 11,369–11,382, doi:10.1029/93JA00605.

Arnoldy, R. L., et al. (2005), Pc1 waves and associated unstable distributions of magnetospheric protons observed during a solar wind pressure pulse, *J. Geophys. Res.*, *110*, A07229, doi:10.1029/2005JA011041.

Bendat, J. S., and A. G. Piersol (2010), *Random Data: Analysis and Measurement Procedures*, John Wiley, N. J.

Clausen, L. B. N., J. B. H. Baker, J. M. Ruohoniemi, and H. J. Singer (2011), EMIC waves observed at geosynchronous orbit during solar minimum: Statistics and excitation, *J. Geophys. Res.*, *116*, A10205, doi:10.1029/2011JA016823.

Cornwall, J. M. (1965), Cyclotron instabilities and electromagnetic emission in the ultra low frequency and very low frequency ranges, *J. Geophys. Res.*, *70*(1), 61–69, doi:10.1029/JZ070i001p00061.

Cornwall, J. M., F. V. Coroniti, and R. M. Thorne (1970), Turbulent loss of ring current protons, *J. Geophys. Res.*, *75*(25), 4699–4709, doi:10.1029/JA075i025p04699.

Darrouzet, F., J. De Keyser, P. M. E. Decreau, F. El Lemdani-Mazouz, and X. Vallieres (2008), Statistical analysis of plasmaspheric plumes with Cluster/WHISPER observations, *Ann. Geophys.*, *26*(8), 2403–2417.

Engebretson, M. J., W. K. Peterson, J. L. Posch, M. R. Klatt, B. J. Anderson, C. T. Russell, H. J. Singer, R. L. Arnoldy, and H. Fukunishi (2002), Observations of two types of Pc 1-2 pulsations in the outer dayside magnetosphere, *J. Geophys. Res.*, *107*(A12), 1451, doi:10.1029/2001JA000198.

Erlandson, R. E., and A. J. Ukhorskiy (2001), Observations of electromagnetic ion cyclotron waves during geomagnetic storms: Wave occurrence and pitch angle scattering, *J. Geophys. Res.*, *106*(A3), 3883–3895, doi:10.1029/2000JA000083.

Fowler, R. A., B. J. Kotick, and R. D. Elliott (1967), Polarization analysis of natural and artificially induced geomagnetic micropulsations, *J. Geophys. Res.*, *72*(11), 2871–2883, doi:10.1029/JZ072i011p02871.

Fraser, B. J. (1985), Observations of ion cyclotron waves near synchronous orbit and on the ground, *Space Sci. Rev.*, *42*, 357–374, doi:10.1007/BF00214993.

Fraser, B. J., and T. S. Nguyen (2001), Is the plasmapause a preferred source region of electromagnetic ion cyclotron waves in the magnetosphere?, *J. Atmos. Sol. Terr. Phys.*, *63*, 1225–1247, doi:10.1016/S1364-6826(00)00225-X.

Fraser, B. J., W. J. Kemp, and D. J. Webster (1989), Ground-satellite study of a Pc 1 ion cyclotron wave event, *J. Geophys. Res.*, *94*(A0), 11,855–11,863, doi:10.1029/JA094iA09p11855.

Fraser, B. J., H. J. Singer, W. J. Hughes, J. R. Wygant, R. R. Anderson, and Y. D. Hu (1996), CRRES Poynting vector observations of electromagnetic ion cyclotron waves near the plasmapause, *J. Geophys. Res.*, *101*(A7), 15,331–15,343, doi:10.1029/95JA03480.

Fraser, B. J., R. S. Grew, S. K. Morley, J. C. Green, H. J. Singer, T. M. Loto'aniu, and M. F. Thomsen (2010), Storm time observations of electromagnetic ion cyclotron waves at geosynchronous orbit: GOES results, *J. Geophys. Res.*, *115*, A05208, doi:10.1029/2009JA014516.

Fraser, B. J., S. K. Morley, R. S. Grew, and H. J. Singer (2012), Classification of Pc1-2 electromagnetic ion cyclotron waves at geosynchronous orbit, in *Dynamics of the Earth's Radiation Belts and Inner Magnetosphere, Geophys. Monogr. Ser.*, vol. 199, edited by D. Summers et al., pp. 53–68, AGU, Washington, D. C., doi:10.1029/2012GM001353

Halford, A. J., B. J. Fraser, and S. K. Morley (2010), EMIC wave activity during geomagnetic storm and nonstorm periods: CRRES results, *J. Geophys. Res.*, *115*, A12248, doi:10.1029/2010JA015716.

Horne, R. B. (2002), The contribution of wave-particle interactions to electron loss and acceleration in the Earth's radiation belts during geomagnetic storms, in *URSI Review of Radio Science 1999–2002*, edited by W. R. Stone, pp. 801–828, Wiley, New York.

Horne, R. B., and R. M. Thorne (1994), Convective instabilities of electromagnetic ion cyclotron waves in the outer magnetosphere, *J. Geophys. Res.*, *99*(A9), 17,259–17,273, doi:10.1029/94JA01259.

Hu, Y. D., and B. J. Fraser (1994), Electromagnetic ion cyclotron wave amplification and source regions in the magnetosphere, *J., Geophys. Res.*, *99*(A1), 263–272, doi:10.1029/93JA01897.

Hyun, K., K.-H. Kim, E. Lee, H.-J. Kwon, D.-H. Lee, and H. Jin (2014), Loss of geosynchronous relativistic electrons by EMIC wave scattering under quiet geomagnetic conditions, *J. Geophys. Res. Space Physics*, *119*, 8357–8371, doi:10.1002/2014JA020234.

Ishida, J., S. Kokubun, and R. L. McPherron (1987), Substorm effects on spectral structures of Pc 1 waves at synchronous orbit, *J. Geophys. Res.*, *92*(A1), 143–158, doi:10.1029/JA092iA01p00143.

Kang, S.-B., K.-W. Min, M.-C. Fok, J. Hwang, and C.-R. Choi (2015), Estimation of pitch angle diffusion rates and precipitation time scales of electrons due to EMIC waves in a realistic field model, *J. Geophys. Res. Space Physics*, *120*, 8529–8546, doi:10.1002/2014JA020644.

Keika, K., K. Takahashi, A. Y. Ukhorskiy, and Y. Miyoshi (2013), Global characteristics of electromagnetic ion cyclotron waves: Occurrence rate and its storm dependence, *J. Geophys. Res. Space Physics*, *118*, 4135–4150, doi:10.1002/jgra.50385.

Kennel, C. F., and H. E. Petschek (1966), Limit on stably trapped particle fluxes, *J. Geophys. Res.*, *71*(1), 1–28, doi:10.1029/JZ071i001p00001.

Kim, K.-H., K. Shiokawa, I. R. Mann, J.-S. Park, H.-J. Kwon, K. Hyun, H. Jin, and M. Connors (2016), Longitudinal frequency variation of long-lasting EMIC Pc1-Pc2 waves localized in the inner magnetosphere, *Geophys. Res. Lett.*, *43*, 1039–1046, doi:10.1002/2015GL067536.

Kozyra, J. U., T. E. Cravens, F. Nagy, E. G. Fontheim, and R. S. B. Ong (1984), Effects of energetic heavy ions on electromagnetic ion cyclotron wave generation in the plasmapause region, *J. Geophys. Res.*, *89*(A4), 2217–2233, doi:10.1029/JA089iA04p02217.

Kwon, H.-J., K.-H. Kim, G. Jee, J.-S. Park, H. Jin, and Y. Nishimura (2015), Plasmapause location under quiet geomagnetic conditions ($Kp \leq 1$): THEMIS observations, *Geophys. Res. Lett.*, *42*, doi:10.1002/2015GL066090.

LaBelle, J., R. A. Treumann, W. Baumjohann, G. Haerendel, N. Sckopke, G. Paschmann, and H. Luhr (1988), The duskside plasmapause/ring current interface: Convection and plasma wave observations, *J. Geophys. Res.*, *93*(A4), 2573–2590, doi:10.1029/JA093iA04p02573.

Loto'aniu, T. M., B. J. Fraser, and C. L. Waters (2005), Propagation of electromagnetic ion cyclotron wave energy in the magnetosphere, *J. Geophys. Res.*, *110*, A07214, doi:10.1029/2004JA010816.

Mauk, B. H. (1982), Helium resonance and dispersion effects on geostationary Alfvén/ion cyclotron waves, *J. Geophys. Res.*, *87*(A11), 9107–9119, doi:10.1029/JA087iA11p09107.

McFadden, J. P., C. W. Carlson, D. Larson, J. Bonnell, F. S. Mozer, V. Angelopoulos, K.-H. Glassmeier, and U. Auster (2008), Structure of plasmaspheric plumes and their participation in magnetopause reconnection: First results from THEMIS, *Geophys. Res. Lett.*, *35*, L17S10, doi:10.1029/2008GL033677.

Meredith, N. P., R. M. Thorne, R. B. Horne, D. Summers, B. J. Fraser, and R. R. Anderson (2003), Statistical analysis of relativistic electron energies for cyclotron resonance with EMIC waves observed on CRRES, *J. Geophys. Res.*, *108*(A6), 1250, doi:10.1029/2002JA009700.

Meredith, N. P., R. B. Horne, T. Kersten, B. J. Fraser, and R. S. Grew (2014), Global morphology and spectral properties of EMIC waves derived from CRRES observations, *J. Geophys. Res. Space Physics*, *119*, 5328–5342, doi:10.1002/2014JA020064.

Min, K., J. Lee, K. Keika, and W. Li (2012), Global distribution of EMIC waves derived from THEMIS observations, *J. Geophys. Res.*, *117*, A05219, doi:10.1029/2012JA017515.

Miyoshi, Y., K. Sakaguchi, K. Shiokawa, D. Evans, J. Albert, M. Connors, and V. Jordanova (2008), Precipitation of radiation belt electrons by EMIC waves, observed from ground and space, *Geophys. Res. Lett.*, *35*, L23101, doi:10.1029/2008GL035727.

Nomura, R., K. Shiokawa, V. Pilipenko, and B. Shevtsov (2011), Frequency-dependent polarization characteristics of Pc1 geomagnetic pulsations observed by multipoint ground stations at low latitudes, *J. Geophys. Res.*, *116*, A01204, doi:10.1029/2010JA015684.

Olson, J. V., and L. C. Lee (1983), Pc1 wave generation by sudden impulses, *Planet. Space Sci.*, *31*(3), 295–302, doi:10.1016/0032-0633(83)90079-X.

Omura, Y., and Q. Zhao (2012), Nonlinear pitch angle scattering of relativistic electrons by EMIC waves in the inner magnetosphere, *J. Geophys. Res.*, *117*, A08227, doi:10.1029/2012JA017943.

Omura, Y., J. Pickett, B. Grison, O. Santolik, I. Dandouras, M. Engebretson, P. M. E Decreau, and A. Masson (2010), Theory and observation of electromagnetic ion cyclotron chorus emissions in the magnetosphere, *J. Geophys. Res.*, *115*, A07234, doi:10.1029/2010JA015300.

Park, J.-S., K.-H. Kim, K. Shiokawa, D.-H. Lee, E. Lee, H.-J. Kwon, H. Jin, and G. Jee (2016), EMIC waves observed at geosynchronous orbit under quiet geomagnetic conditions ($K_p \leq 1$), *J. Geophys. Res. Space Physics*, *121*, 1377–1390, doi:10.1002/2015JA021968.

Rodger, C. J., M. A. Clilverd, J. C. Green, and M. M. Lam (2010), Use of POES SEM-2 observations to examine radiation belt dynamics and energetic electron precipitation into the atmosphere, *J. Geophys. Res.*, *115*, A04202, doi:10.1029/2008JA014023.

Shoji, M., and Y. Omura (2013), Triggering process of electromagnetic ion cyclotron rising tone emissions in the inner magnetosphere, *J. Geophys. Res. Space Physics*, *118*, 5553–5561, doi:10.1002/jgra.50523.

Shprits, Y. Y., W. Li, and R. M. Thorne (2006), Controlling effect of the pitch angle scattering rates near the edge of the loss cone on electron lifetimes, *J. Geophys. Res.*, *111*, A12206, doi:10.1029/2006JA011758.

Shprits, Y. Y., D. Subbotin, A. Drozdov, M. E. Usanova, A. Kellerman, K. Orlova, D. N. Baker, D. L. Turner, and K. C. Kim (2013), Unusual stable trapping of the ultra-relativistic electrons in the Van Allen radiation belts, *Nat. Phys.*, *9*(11), 699–703, doi:10.1038/nphys2760.

Sugiyama, H., S. Singh, Y. Omura, M. Shoji, D. Nunn, and D. Summers (2015), Electromagnetic ion cyclotron waves in the Earth's magnetosphere with a kappa-Maxwellian particle distribution, *J. Geophys. Res. Space Physics*, *120*, 8426–8439, doi:10.1002/2015JA021346.

Summers, D., and R. M. Thorne (2003), Relativistic electron pitch-angle scattering by electromagnetic ion cyclotron waves during geomagnetic storms, *J. Geophys. Res.*, *108*(A4), 1143, doi:10.1029/2002JA009489.

Thorne, R. M., and C. F. Kennel (1971), Relativistic electron precipitation during magnetic storm main phase, *J. Geophys. Res.*, *76*(19), 4446–4453, doi:10.1029/JA076i019p04446.

Usanova, M. E., I. R. Mann, I. J. Rae, Z. C. Kale, V. Angelopoulos, J. W. Bonnell, K. H. Glassmeier, H. U. Auster, and H. J. Singer (2008), Multipoint observations of magnetospheric compression-related EMIC Pc1 waves by THEMIS and CARISMA, *Geophys. Res. Lett.*, *35*, L17S25, doi:10.1029/2008GL034458.

Usanova, M. E., I. R. Mann, J. Bortnik, L. Shao, and V. Angelopoulos (2012), THEMIS observations of electromagnetic ion cyclotron wave occurrence: Dependence on AE, SYMH, and solar wind dynamic pressure, *J. Geophys. Res.*, *117*, A10218, doi:10.1029/2012JA018049.

Usanova, M. E., et al. (2014), Effect of EMIC waves on relativistic and ultra-relativistic electron populations: Ground-based and Van Allen Probes observations, *Geophys. Res. Lett.*, *41*, 1375–1381, doi:10.1002/2013GL059024.

Yahnina, T. A., A. G. Yahnin, J. Kangas, and J. Manninen (2000), Proton precipitation related to Pc1 pulsations, *Geophys. Res. Lett.*, *27*(21), 3575–3578, doi:10.1029/2000GL003763.

Yuan, Z., Y. Xiong, D. Wang, M. Li, X. Deng, A. G. Yahnin, T. Raita, and J. Wang (2012), Characteristics of precipitating energetic ions/electrons associated with the wave-particle interaction in the plasmaspheric plume, *J. Geophys. Res.*, *117*, A08324, doi:10.1029/2012JA017783.

Young, D. T., S. Perraut, A. Roux, C. de Villedary, R. Gendrin, A. Korth, G. Kremser, and D. Jones (1981), Wave-particle interactions near $\Omega_{He^+}$ observed on GEOS 1 and 2: 1. Propagation of ion cyclotron waves in He$^+$-rich plasma, *J. Geophys. Res.*, *86*(A8), 6755–6772, doi:10.1029/JA086iA08p06755.